photonics

MDPI

Article

Characterization of Cubic Zirconia as a Lens Material Suitable for Autonomous Driving

Jae-Kun Lee [1], Sung Yun Chung [2], Eui Chul Shin [1], Jae Bum Kim [3] and Jong-Kwon Lee [2,*]

[1] DSM Co., Ltd., Anseong 17553, Korea
[2] Division of Energy and Optical Technology Convergence, Cheongju University, Cheongju 28503, Korea
[3] Optical Research Center, Optrontec, Sungnam 13486, Korea
* Correspondence: jklee7@cju.ac.kr

Abstract: As the development of autonomous driving technology is now in full swing, the demand for miniaturized optical modules mounted on various sensors has increased. Particularly, the optical lens used for such autonomous driving must demonstrate stable performance and durability despite rapid changes in the external environment. In this regard, cubic zirconia (CZ) can be used as an optical lens due to its high refractive index, which is above 2.1 in visible and near-infrared wavelengths, along with its chemical and mechanical durability. Thus, in this paper, we investigated the temperature-dependent physical properties of CZ fabricated by the skull melting method. The temperature coefficient of the refractive index (*dn/dT*) of the fabricated CZ plate in the temperature range of 25–100 °C decreased from 9.76×10^{-5}/K to 7.00×10^{-5}/K as the wavelength increased from 447.0 nm to 785.0 nm. The estimated Abbe number decreased from 33.98 at 25 °C to 33.12 at 100 °C, while the measured coefficient of thermal expansion (CTE) was 9.91×10^{-6}/K, which revealed that the *dn/dT* value of the CZ plate was more affected by the dispersion than by the CTE. In addition, the CZ samples with a high refractive index, coated with a dielectric multilayer showed a high average transmittance of 98.2% at the investigated wavelengths, making it suitable for miniaturization or wide-angle optical lens modules. To secure the durability required for automobile lenses, the variation in the surface profile of the CZ before and after the external impact was also analyzed, revealing much better performance than TAF glass. Therefore, the observed results demonstrate that the CZ material is suitable for use as an optical lens for autonomous vehicles.

Keywords: cubic zirconia; high refractive index; thermo-optic property; impact strength; autonomous driving

Citation: Lee, J.-K.; Chung, S.Y.; Shin, E.C.; Kim, J.B.; Lee, J.-K. Characterization of Cubic Zirconia as a Lens Material Suitable for Autonomous Driving. *Photonics* **2022**, *9*, 701. https://doi.org/10.3390/photonics9100701

Received: 25 July 2022
Accepted: 24 September 2022
Published: 28 September 2022

1. Introduction

With the recent advances in artificial intelligence technology, it is becoming possible to classify, interpret and respond to objects based on various optical information obtained through optical lenses [1,2]. Thus, optical lenses are considered a core element of various advanced technologies such as autonomous driving, augmented and virtual reality, drones and robots [3,4]. In particular, autonomous vehicle technology, which has recently attracted attention, is being implemented in the form of an Advanced Driver Assistance System (ADAS). This ADAS detects external environment information from various sensors and cameras mounted on a vehicle and informs the driver to take appropriate action or provides a safe driving environment through the vehicle's own driving controls [5]. The main sensors adopted in the ADAS are cameras, radars, ultrasonic sensors and LiDARs [5,6]. Among them, optical filters and lenses with excellent performance are essential for cameras and LiDARs. LiDAR sensors detect an object by shining light on a target and then measuring the reflected signal and have to transmit and receive light quickly in multiple directions; therefore, dozens of lenses are usually included in one sensor. Unlike radar, which uses radio waves, cameras and LiDARs that use visible and NIR wavelengths, respectively, are also affected by external pollution such as dust and muddy water [6,7].

In contrast to current smartphone cameras, which are equipped with lightweight plastic lenses, glass-based materials are mainly adopted in automotive cameras and sensors to secure good performance in a relatively high-temperature environment [3]. Thus, it is necessary to design camera lens modules for automobiles to withstand extreme environmental conditions such as water, low temperatures of −40 °C and high temperature up to 100 °C [3]. In addition, the optical lens has to withstand possible external shocks (by atmospheric dust or small stones that bounce off nearby vehicles) and bad weather. Clear visibility is also required both at night and during the day by improving aberration in the visible to the NIR range [3,8]. Moreover, the temperature increase causes variations in the refractive indices of the optical lens and also expands the lens material. Thus, the optical lenses for automobiles should be manufactured while considering both the temperature coefficient of the refractive index (*dn/dT*) and the coefficient of thermal expansion (CTE) to meet the strict requirements for very high performance and high reliability. Currently, the commercial Ohara's glass used for in-vehicle camera lens is S-LHA52Q with a large *dn/dT* of 10.3, S-LAL20 with minus *dn/dT* of −1.2 (@*d*-line 40 °C~60 °C), and S-LAL50Q with improved mechanical strength and chemical stability [8]. Additionally, Hoya Corporation has released M-PCD55AR with an acid resistance 1 grade and a small refractive index temperature change (*dn/dT*) suitable for automotive camera lens [9].

High-purity oxide ceramics with a cubic structure exhibit transparency comparable to optical glasses and single crystals. Additionally, they have inherent ceramic characteristics such as high mechanical strength and surface hardness, chemical stability and wear resistance [10,11]. These properties of oxide ceramics allow the use of transparent ceramics in a variety of harsh environments and operating conditions [11,12]. Especially, cubic zirconia (CZ) ceramics show a higher refractive index of above 2.1 at visible and NIR wavelengths than optical glasses [13,14], which allows the implementation of small or compact lens systems with wide-angle features. They also exhibit relatively high mechanical properties compared to other ceramic materials and are stable in a chemically corrosive environment with a low thermal conductivity of 3 W/(mK) and high fire resistance with a melting point of 2750 °C [15,16]. Thus, the high refractive index and high durability of CZ materials compared with other transparent materials are expected to be utilized in high-refractive-index lenses for optoelectronic devices and infrared windows [16,17]. In this respect, there have been reports on the structural and optical properties of zirconium oxide (ZrO_2) nanoparticles [18] and zirconia thin films [13], as well as the electronic, optical and elastic properties of CZ ceramic under pressure [15]. Skull melting and sintering methods have been widely adopted to obtain CZ ceramics from the raw material, zirconia. Table 1 compares the characteristics of various CZ production technologies and cites the references related to the physical properties of the CZ ceramics fabricated by each method.

Meanwhile, when the cameras' optical systems are exposed to various thermal environments, the change in the refractive index of the lens results in a shift in the focal point, leading to failure to capture clear images. Thus, the dependence of the refractive index on temperature (*dn/dT*) and the wavelength dispersion are two important parameters that affect the design of the optical system installed in in-line vehicles. Nevertheless, there have been few reports on the thermal variation in the refractive index and the dispersion of CZ materials along with their resistance to external impacts for automotive applications.

In this paper, we explored the temperature-dependent physical properties of CZ from ZrO_2 containing Y_2O_3, which was manufactured by the skull melting method. We firstly investigated the transmittance spectra of the fabricated CZ ceramics with or without an anti-reflection (AR) layer. This AR layer is essential to achieve high transmittance by reducing the surface reflectance of the CZ ceramic with a high refractive index. Then, the change in the refractive index (*dn/dT*) and the dispersion characteristics of the CZ material according to the temperature were analyzed in the visible and NIR wavelength regions. The observed results were then explained in relation to the measured thermal expansion coefficient and the temperature coefficient of the optical path length of the CZ materials. Finally, we carried

out an impact test on the surface of the CZ ceramics to assess the mechanical stability under external shock.

Table 1. Comparison of CZ production technologies along with relevant references.

Methods	Characteristics	Refs.*
Skull Melting	A water-cooled, Cu crucible-like structure is used to surround the RF-heated molten zirconia. The temperature of this process reaches 3000 °C or higher. It produces high-purity CZ ceramics without pores due to no contact of the melt with the crucible materials [19].	[20–23]
Spark Plasma Sintering	The powder materials are stacked between the die and punch on the sintering stage and held between the electrodes. Under pressure and pulse energized, the temperature quickly rises to 1000~2500 °C, producing a high-quality sintered compact in a few mins [24].	[25–30]
Hot Pressing	Milling, forging and extrusion are performed at high temperature and pressure. It is a uniaxial-pressure, low-strain-rate powder metallurgy process to form powders at a temperature enough to induce sintering and creep processes by the simultaneous application of heat and pressure [31].	[32–34]
Hot Isostatic Pressing	Material is compressed by simultaneously applying high temperature (several hundreds to 2000 °C) and isostatic pressure (several tens to 200 MPa) using gas pressure. A commonly used pressure medium is Argon. Produced material shapes similar to the initial one after pressure [34,35].	[36–38]
Cold Pressing and Fusion	This is an unusually low-temperature process utilizing a transient transport phase and it applies uniaxial force to assist in densification of a powder compact. Many ceramic powders can be transformed to high-density monoliths at temperatures below the melting point [39].	[40–42]

Ref.*: References related to the physical properties of CZ ceramics fabricated by each method.

2. Materials and Methods

2.1. Fabrication and Phase Analysis of Cubic Zirconia Samples

ZrO_2 and Y_2O_3 with an 80:20 atomic ratio were used for fabricating the CZ ceramics. Both the ZrO_2 and Y_2O_3 are products of Terio (Qingdao Terio Co. China www.terio.cn (accessed on 8 July 2022), the purity is over 99.995% and the D_{50} particle size is less than 1 μm. The weighted powders were wet-mixed for 20 h in a jar containing zirconia balls and ethanol, and the slurry was then completely dried in an oven. These CZ ceramics were obtained by the skull melting method for mixed powders, and the total amount of mixed powder in one batch was 30 kg. The skull used had a crucible diameter of 200 mm and a crucible height of 300 mm. To obtain crystal from a ceramic, the materials must be melted. Pure zirconia has a very high melting point at 2750 °C and platinum or ceramic crucibles cannot withstand the heat. For the melting, radio-frequency (RF) driving conditions such as a total electric input power of 85 kW and frequency of 850 kHz were used with the skull crucible. Here, we adopted a vacuum tube (ITK 15-2) with an RF output power of 50 kW and tank condenser capacitor of 20,000 pF, and the oscillation type was Hartrey. The skull melting process utilized a water-cooled copper crucible structure to enclose the RF-heated molten zirconia contained in a thin shell of its own composition as shown in Figure 1a. The temperature for the skull melting reached 3000 °C, and the growth rate was around 5.0 mm/h. The sequence of electric parameters of the CZ skull melting furnace in the process of melting, soaking and crystallization is presented in Table 2 in detail. Several

samples obtained by processing the fabricated CZ materials are shown in Figure 1b. Then, the phase of the fabricated CZ ceramics was analyzed by using X-ray diffraction (XRD) (Panalytical X'Pert Pro MRD high-resolution diffractometer, Malvern, Spain) with an X-ray source of Cu Kα radiation (λ = 1.5406 Å) produced at 40 kV and 30 mA. The diffraction angle (2θ) was scanned between 10° and 70° with a step size of 0.026° at 2θ per second. Figure 1c shows the XRD pattern of the fabricated CZ sample compared to the index data (PDF # # 01-089-9069 of ZrO_2). The measured diffraction peaks match the indexed peaks, revealing the cubic phase with a lattice parameter of 0.5139 nm at room temperature, as previously reported [43–45].

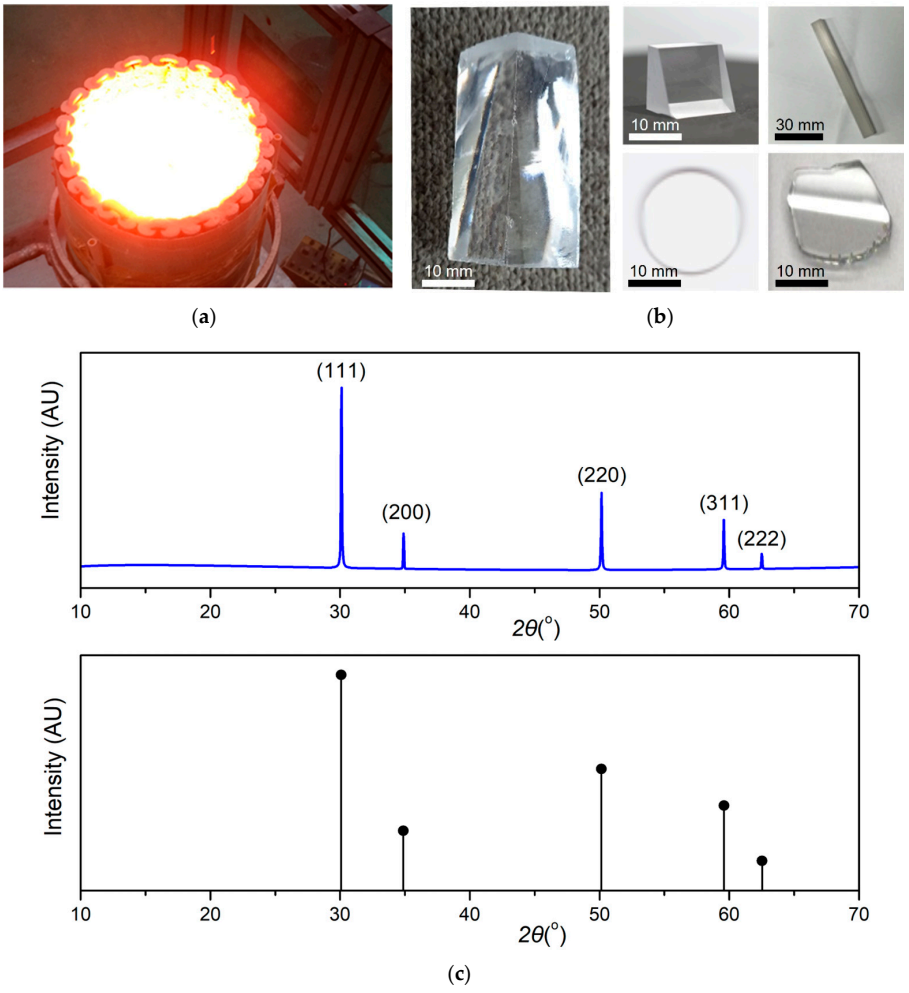

Figure 1. (**a**) Picture of the skull melting furnace used to crystallize cubic zirconia; (**b**) Pictures of the samples processed and polished with the cubic zirconia fabricated by the skull melting method; (**c**) XRD pattern of the fabricated CZ sample compared to the index data (PDF # 01-089-9069 of ZrO_2).

Table 2. The sequence of electrical parameters in the melting, soaking and crystallization process to fabricate the cubic zirconia in the skull melting furnace.

Process	Operation Time (hrs.)	Condition of Radio Frequency				
		Power (kW)	Freq. (kHz)	Ea * (kV)	Ia ** (A)	Ig *** (A)
Melting	1	20	840→850	6→12	3.5→6	0.3→0.5
Soaking	3	50	850	10	6	0.45
Growing	20	50	850→890	10→9	6→7.5	0.35
Cooling	24	-	-	-	-	-

Ea *: Anode voltage (kV), Ia **: Anode current (A), Ig ***: Grid current (A).

2.2. Transmittance Measurement of the Fabricated CZs

Diffuse transmittance of the fabricated CZ samples with a 5 mm thickness and a 19 mm diameter was measured by a UV-Visible spectrophotometer (V-770 EX, Jasco, Tokyo, Japan) in the wavelength range of 300 nm to 1800 nm. Then, to achieve high transmittance (above 98%) of the CZ samples with a high refractive index, antireflection (AR) multilayers consisting of SiO_2 (86.8 nm)/TiO_2 (112.9 nm)/ SiO_2 (47.8 nm)/ TiO_2 (14.9 nm)/ SiO_2 (73.1 nm)/ TiO_2 (20.5nm)/SiO_2 (23.5 nm) at a reference wavelength of 510 nm were coated on the surface of the CZ sample at visible range for camera lens applications. Meanwhile, AR multilayers with SiO_2 (204.1 nm)/TiO_2 (282.9 nm)/SiO_2 (97.9 nm)/TiO_2 (49.5 nm)/SiO_2 (134.9 nm)/TiO_2 (52.4 nm)/ SiO_2 (50.3 nm) at a reference wavelength of 1200 nm were deposited on the CZ samples at NIR range for LiDAR application. These AR coating layers were deposited by an e-beam evaporator (HVC-1400, Hanil Vacuum Co., Incheon, Korea) under the conditions of maintaining a vacuum at 250 °C and a pressure of 2.0×10^{-5}.

2.3. The Effect of Temperature on Refractive Index and Dispersion of CZ Ceramics

The refractive index variations in the CZ material according to the temperature change from 25 °C to 100 °C were measured using a prism coupler (2010/M MODEL, METRICON, Pennington, NJ, USA). The CZ sample with a thickness of 5 mm was placed in contact with the base of the prism with a pneumatic coupling head. By rotating the prism and the CZ sample placed on a computer-driven rotation table, the change in the intensity of light coming from the right inclined surface of the prism was measured with a detector according to the incident angle of laser light impinging on the left inclined surface of the prism. Here, the refractive index of the CZ material was determined by measuring the critical angle at which total reflection occurred in the prism base. The wavelengths of the lasers used in the experiment were 447.0 nm, 532.0 nm, 632.5 nm and 785.0 nm. Here, the measurements of the dispersions depending on temperature were performed at 25 °C, 50 °C, 75 °C and 100 °C, respectively, and then the temperature–refraction coefficients at each wavelength were measured.

2.4. Measurement of the Coefficient of Thermal Expansion of the CZ Materials

The thermal expansion of the CZ sample, measuring 7 mm × 7 mm × 72 mm, was measured using a push-rod type dilatometer (DIL 402C, NETZSCH) under a gas flow rate of 50 mL/min. Here, the heating rate was 5 °C/min within the range from 5 °C to 500 °C, and the contact force of the push-rod was 0.1 N. Then, the CTE was obtained by calibrating the measured data with a fused silica standard.

2.5. External Impact Test on the CZ Materials

To evaluate the resistance to external impact caused by small stones, dust, etc., cold iron particles (size: 0.33 g iron particles, total 500 g), adopted according to ISO 4287 and 4288 conditions, were collided with the sample surface to perform the test. The resistance of the CZ sample (with a thickness of 5 mm) to external impact was compared with that of TAF glass with the same thickness. To quantitatively evaluate the resistance to external impact, the difference in the changes in the surface roughness of the two samples before and after the impact was measured using a surface analysis system (KLA-Tencor. Co., D-300, Milpitas, CA, USA).

3. Results and Discussion

The CZ ceramics produced by the skull melting method were processed and polished in a form (as shown in Figure 1b) suitable for the evaluation of the optical and mechanical properties according to temperature. These samples were utilized to investigate the transmittance, temperature-dependent dispersion, thermo-optic coefficient and thermo-mechanical coefficient, as well as the surface roughness variation before and after the external impact on the CZ samples as follows.

3.1. Transmittance Characteristics of the Fabricated CZ Samples in Visible to NIR Range

The transparent window for most dielectric materials is bounded by the infrared absorption mode of phonons in the long-wavelength region and by interband electron-hole transitions in the short-wavelength region. Since the intrinsic band gap of yttria-stabilized zirconia is ~4.23 eV [46], the absorption edge of the cubic zirconia lies at about 300 nm. Meanwhile, the infrared phonon absorption occurs in the mid IR range [47,48]. Thus, the pure CZ sample shows an almost uniform transparency of ~75% in the visible and NIR wavelength ranges as indicated by the black lines in Figure 2a,b. It is noted that the CZ ceramics show high transparency up to the IR region because of their large dielectric constant due to ionic polarization in comparison with other transparent ceramic materials [45,46]. Nevertheless, the observed large reflectance loss of ~25% from the surface of the pure CZ is attributed to the high refractive index of above 2.1 of the CZ ceramics in the visible and NIR wavelengths. To improve the transmittance in these wavelengths, the CZ samples were coated with a dielectric multilayer consisting of SiO_2 (low refractive index) and TiO_2 (high refractive index) as shown in Figure 2c,d, which reveals that the transparency of the CZ sample is significantly increased, as indicated by the red lines in Figure 2a,b. The observed average transmittance of double-side AR coating is 98.2% in both the visible and NIR ranges. Here, the transmittance of below 90% observed in the wavelength less than 420 nm (Figure 2a) and the wavelength range between 700 nm and 900 nm (Figure 2b) is attributed to the multilayer coating condition. In addition, the degree of improvement in the transmittance by applying a single-side or double-side AR coating was compared at visible and NIR wavelengths as shown in Figure 2a,b, respectively.

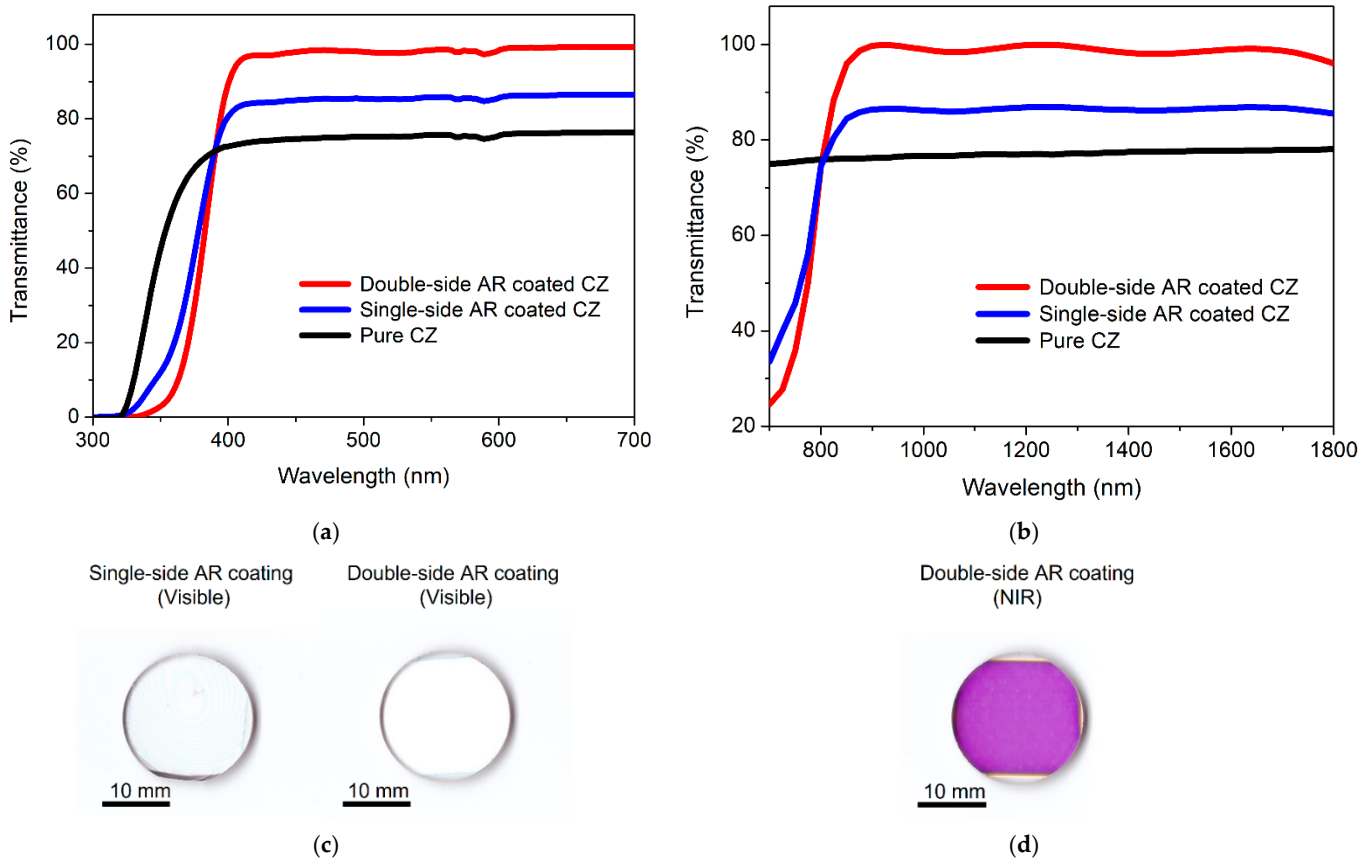

Figure 2. Transmission spectra of the cubic zirconia samples coated with a double-side or single-side AR dielectric multilayer and the pure cubic zirconia sample (**a**) in the visible wavelength and (**b**) NIR wavelength; (**c**,**d**) pictures of the cubic zirconia samples (19 mm diameter and 5 mm thickness) coated with the visible and NIR broadband AR multilayer.

3.2. Dispersion and Temperture Coefficient of the Refractive Index of the Fabricated CZ

To utilize a ceramic material as a lens in a broad wavelength, the dispersion must be small for chromatic aberration correction, and absorption in the corresponding wavelength range must be low to obtain high transparence. In addition, as the refractive index of a lens material increases, the radius of the curvature of the lens surface can be increased to have the same refractive power, leading to reduced aberration of the lens. Moreover, a small change in the refractive index in various thermal environments reduces the aberration imbalance and the focal length changes depending on the temperature, which helps to maintain the performance of the optical system in a wide temperature range. This change in the refractive index according to temperature mainly depends on the change in density caused by the CTE, as well as the increase in polarizability of the material with temperature [48,49].

Figure 3a shows the wavelength dependence of the refractive index values of the fabricated CZ sample at different temperatures of 25 °C, 50 °C, 75 °C and 100 °C. The measured refractive indices at the wavelengths of 447.0 nm, 532.0 nm, 632.8 nm and 785.0 nm are 2.214, 2.1876, 2.1686 and 2.1484 on average at room temperature, respectively, which shows the same trend in dispersion as that in the literature [50,51]. It was also observed that the refractive index of the CZ sample gradually increased as the temperature increases (positive *dn/dT*), which is attributed to the shift in the absorption edge (bandgap) of the material with increasing temperature [50]. Meanwhile, the negative *dn/dT* is mainly caused by the decreased density of materials as the temperature increases [50]. To represent the dispersion of the CZ sample in the visible and NIR wavelength range, we fitted the refractive index values measured at four temperatures of 25 °C, 50 °C, 75 °C and 100 °C by the least square method using the Cauchy equation [52] below.

$$n(\lambda) = A + B/\lambda^2 + C/\lambda^4 \quad (1)$$

where A, B, and C are the Cauchy parameters. For example, the estimated Cauchy parameters of the fabricated CZ sample at room temperature are A = 2.124, B = 0.018 and C = 3.150 × 10^{-5}. To quantitatively estimate the dispersion variation depending on the temperature, we calculated the Abbe's number (v_d) defined by the formula below utilizing the refractive index of the d-line (587.56 nm), F-line (486.1 nm) and C-line (656.3 nm) obtained in Figure 3a.

$$v_d = \frac{n_d - 1}{n_F - n_C} \quad (2)$$

Figure 3b represents the variation in the Abbe number of the CZ sample with temperatures ranging from 25 °C to 100 °C, which was estimated from the average refractive indices of Figure 3a. It was observed that the decrease in the rate of Abbe number (or increase in the rate of dispersion) when the temperature was increased to 50 °C, 75 °C and 100 °C was 0.36%, 2.18% and 2.56%, respectively, with respect to the Abbe number at 25 °C. This means that the variation in the dispersion, according to this temperature range, was much smaller than the material dispersion itself. Figure 3c shows the temperature-dependent refractive index at 447 nm, 532 nm, 632.8 nm and 785 nm for the CZ sample, which reveals that the refractive index monotonically increases as the temperature increases. Then, we estimated the *dn/dT* of the CZ at these wavelengths as shown in Figure 3d. Here, linear fits were applied to the measured data due to the small variation (Δn) in the average refractive index over the temperature range of 25–100 °C. The results show that the temperature coefficients of the refractive index decreased from 9.76 × 10^{-5} to 7.00 × 10^{-5} as the wavelength increased from 447.0 nm to 785.0 nm. The observed temperature coefficients of the fabricated CZ samples show slightly higher values than those of Ohara commercial glass, such as PBH71, PBH-1, and S-BSM16 (4~20 × 10^{-6}) [53], while the CZ ceramic shows a higher refractive index than the commercial glass. Thus, the observed temperature-dependent dispersion and *dn/dT* values indicate that the CZ ceramics can maintain a stable performance in various thermal environments.

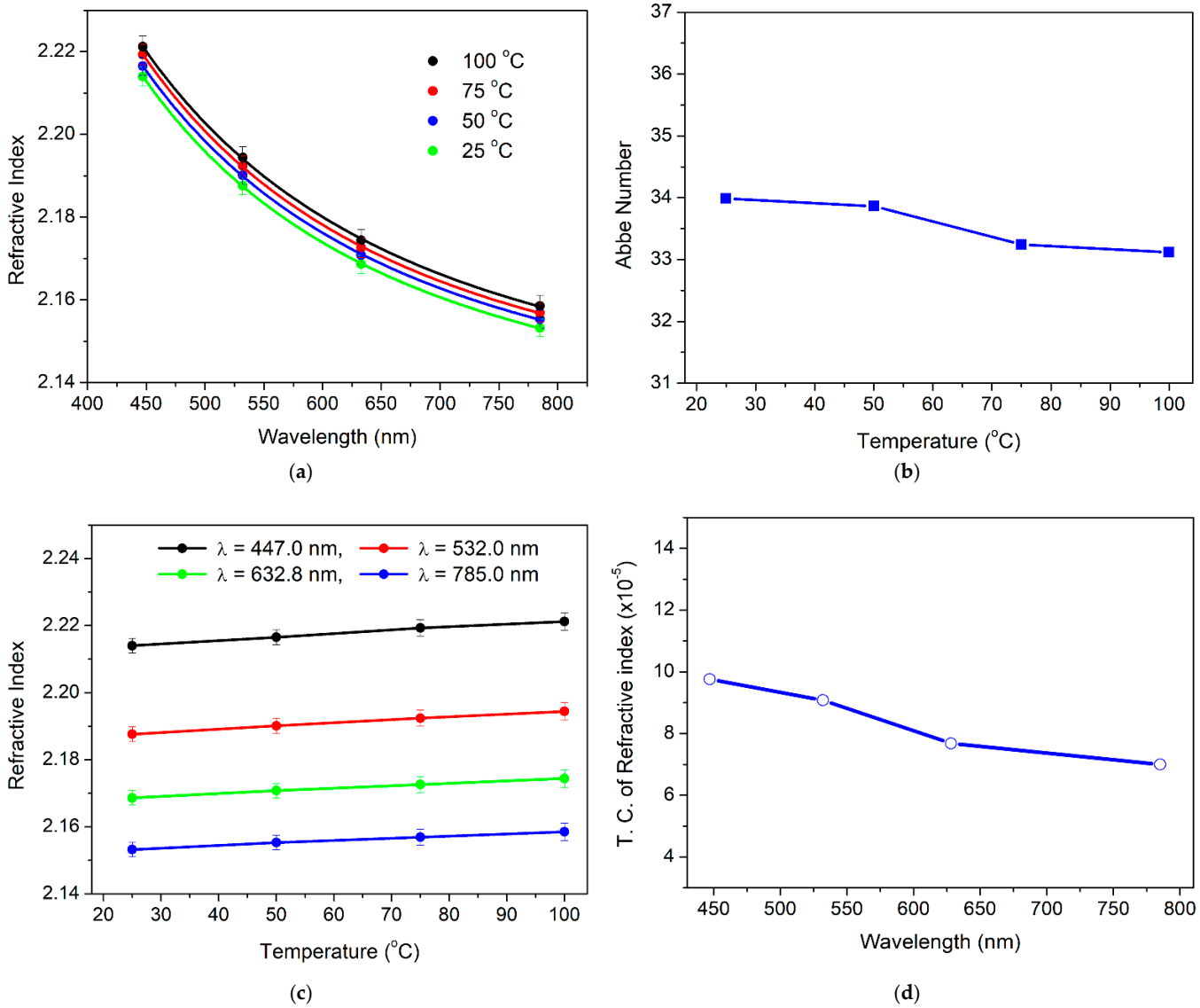

Figure 3. (**a**) Dispersion in the visible and NIR wavelengths of the fabricated CZ sample depending on temperature; (**b**) Abbe number (ν_d) estimated from the average refractive indices in (**a**) as a function of temperature; (**c**) temperature dependence of the refractive indices at 447 nm, 532 nm, 632.8 nm and 785 nm for the CZ sample; (**d**) temperature coefficient of refractive index estimated from the average refractive indices in (**c**) depending on the wavelength.

3.3. The Coefficient of Thermal Expansion of the Fabricated CZ

Figure 4a shows the change in the length of the thermal expansion according to temperatures of 5–500 °C, which were applied to the fabricated CZ sample, which measured 8 mm in diameter and 10 mm in length. It was observed that the elongation of the sample monotonically increased as the temperature increased. Here, the CTE value (α) was estimated to be 9.91 $\times$ 10^{-6}/K from the average values represented in Figure 4a. The thermal expansion of the material changes its refractive index. Thus, we estimated the temperature coefficient of the optical path length (ds/dT) given by the below equation [54] by considering the dn/dT and the CTE of the material.

$$\frac{ds(\lambda)}{dT} = n(\lambda)\,\alpha + \frac{dn(\lambda)}{dT} \tag{3}$$

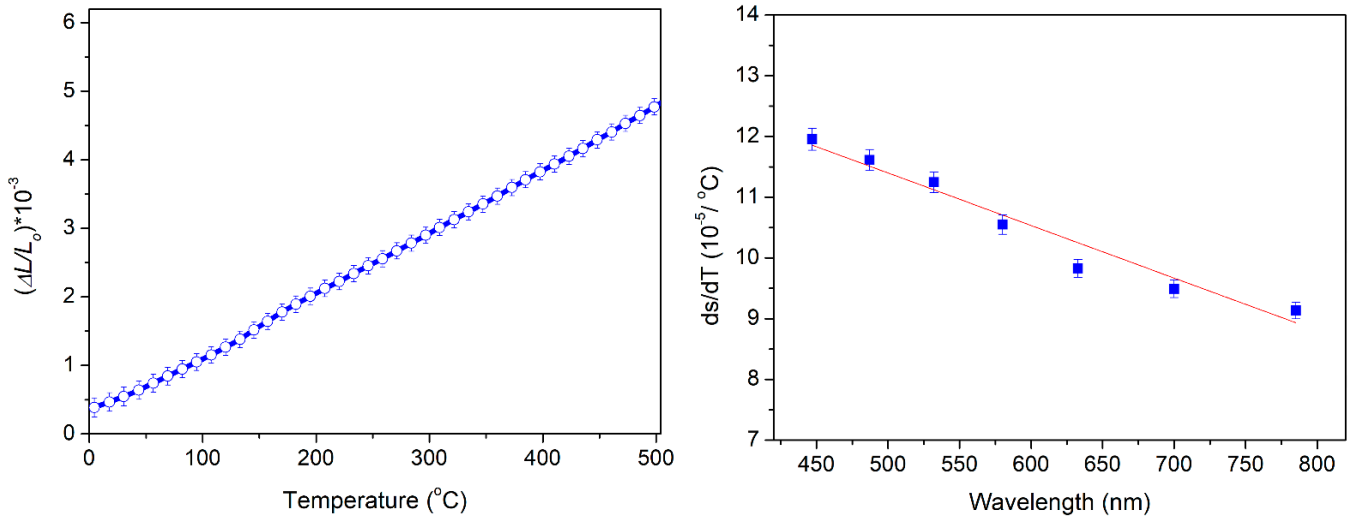

Figure 4. (**a**) The change in the length of thermal expansion for the fabricated CZ plate in the temperature range of 5 °C to 500 °C. (**b**) Temperature coefficient of the optical path length as function of wavelength for the CZ plate, with the linear fit shown by the solid red line.

Figure 4b shows the estimated *ds/dT* of the CZ sample for different wavelengths. A linear decrease in *ds/dT* with the wavelength was observed at the investigated wavelengths. The estimated *ds/dT* includes information about the CTE, electronic polarizability and the refractive index change [53]. Additionally, since the CTE is irrespective of the wavelength, the wavelength dependence of *ds/dT* is related to the wavelength-dependent electronic polarizability of the CZ ceramic. Thus, the polarizability decreased to about 23.6% as the wavelength increased from 447 nm to 785 nm, as shown in the linear fit in Figure 4b. In addition, it is noted that the (*dn/dT*) value is mainly determined by the dispersion and the CTE. Materials with high dispersion show a relatively high *dn/dT* due to a shift in the thermal band gap, whereas a material with a high CTE shows a relatively low *dn/dT* because the atomic density decreases due to thermal expansion [50]. Thus, the observed *dn/dT* values of the fabricated CZ are more affected by the dispersion than by the CTE.

3.4. External Shock Effect on Fabricated CZ

The hardness of the lens surface for vehicle applications must be high to withstand scratching or abrasion and the greater the mechanical strength, the thinner the lens can be while resisting vibration shock. To compare the resistance to external impact of CZ sample with TAF (Tantalum flint) glass, the surface of the two samples was impacted by cold-iron grits. Here, the TAF was selected as a comparison because it has been applied as a commercial lens for automotive vehicles due to its high Knoop hardness (~790 kg/ mm^2) [53,55,56]. Figure 5a,b show the images of the TAF glass and CZ ceramics, respectively, before and after the collision with the cold-iron grits. It is clearly seen that the surface of the TAF glass was severely damaged after the collision, while the CZ has no surface scratches and no defects occurred. To qualitatively compare the degree of resistance to the external impacts, the variations in the surface roughness of the two samples before and after the collision were measured by scanning the surface of the samples at a distance of 0.5 mm, as shown in Figure 5c,d. The average values and the standard deviation of the measured surface roughness are summarized in Table 3. The results show that the surface roughness in the TAF glass significantly increased from 1.59 nm to 1.54 µm on average by three orders of magnitude (Figure 5c), whereas the roughness of the CZ ceramic showed almost no change before and after the external impact (Figure 5d). Here, the difference in the surface roughness of the two materials was confirmed through surface analysis according to ISO 4287 and 4288, before and after the external impact test. Therefore, it was observed

that the CZ ceramic also has good resistance to external impact in comparison with the conventional glass.

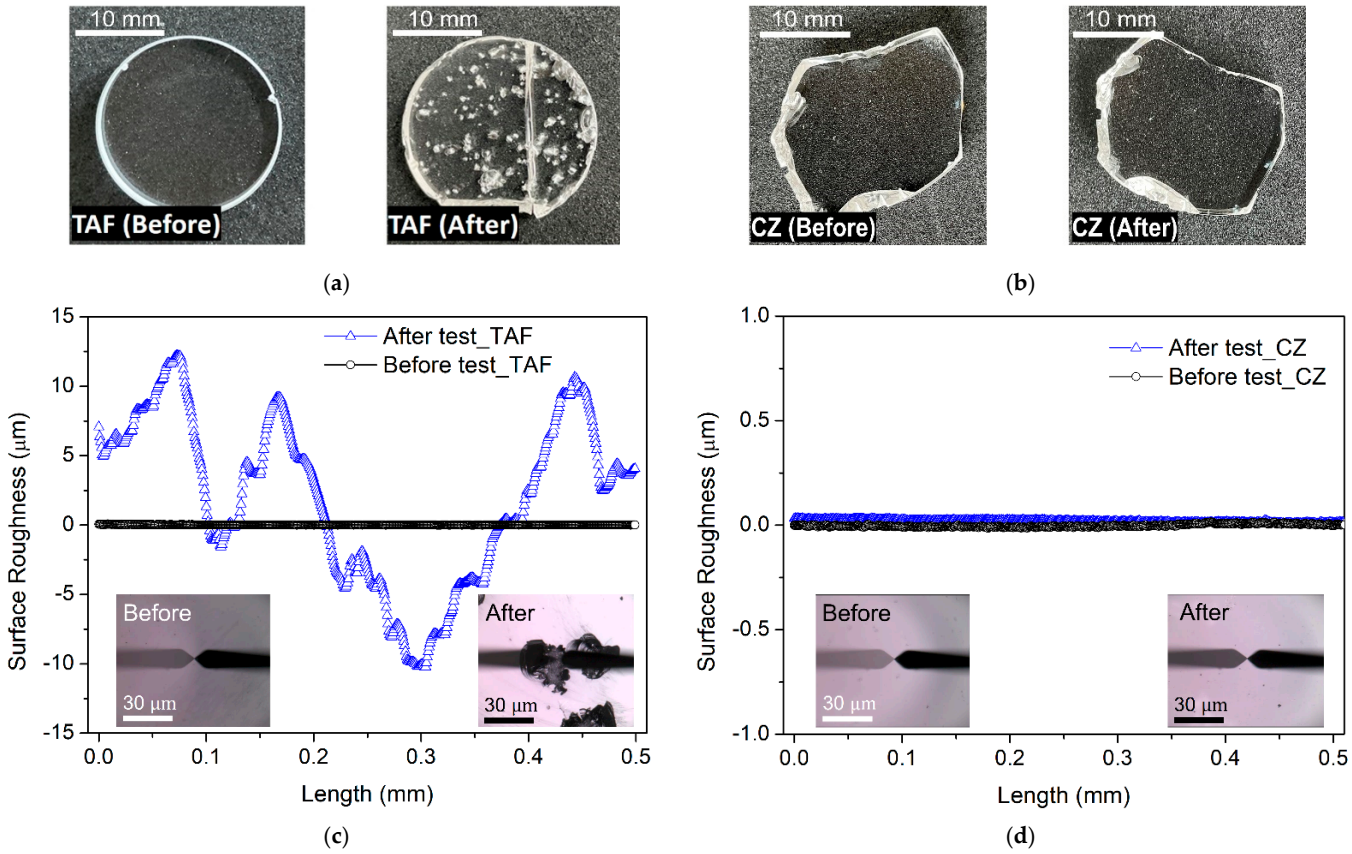

Figure 5. (**a**,**b**) Pictures of the TAF sample and the CZ sample before and after the external impact test; (**c**,**d**) variation in surface roughness (R_a) values of the TAF sample and the CZ sample before and after the external impact test. The inset pictures in (**c**,**d**) were obtained through a surface analysis system.

Table 3. The mean and standard deviation of surface roughness (R_a) value of the TAF glass and the CZ sample before and after the external impact test.

Type	Ave. ± SD *
TAF_Before test	1.59 ± 0.37 nm
TAF_After test	1.54 ± 0.06 μm
CZ_Before test	1.44 ± 0.26 nm
CZ_After test	2.40 ± 0.90 nm

* SD: Standard Deviation.

4. Conclusions

The CZ ceramics fabricated by the skull melting method from a mix of high purity ZrO_2 and Y_2O_3 powders exhibit stable characteristics in regard to the representative optical and mechanical properties according to temperature change. The *dn/dT* of the fabricated CZ ceramic in the temperature range of 25–100 °C varied from 9.76×10^{-5}/K at 447.0 nm to 7.00×10^{-5}/K at 785.0 nm. The estimated Abbe number changed from 33.98 at 25 °C to 33.12 at 100 °C, whereas the CTE of the fabricated CZ was 9.91×10^{-6}/K. The observed results show that the *dn/dT* of the fabricated CZ is more affected by the dispersion than by the CTE. In addition, a high transmittance of 98.2% on average at the visible and NIR wavelengths was achieved by applying an AR dielectric multilayer to the CZ material with a high refractive index. Moreover, the surface roughness of the CZ material after the external

impact test maintained its initial value. Therefore, our research results show that the CZ ceramic is a suitable lens material for realizing compact optical modules with the high durability required in various sensor systems including autonomous driving applications.

Author Contributions: This work was performed through the collaboration of all authors. Conceptualization, J.-K.L. (Jae-Kun Lee) and E.C.S.; methodology, J.-K.L. (Jong-Kwon Lee) and J.B.K.; validation and measurement, E.C.S., J.-K.L. (Jae-Kun Lee) and S.Y.C.; formal analysis and investigation, J.-K.L. (Jae-Kun Lee), S.Y.C., J.B.K. and J.-K.L. (Jong-Kwon Lee); writing—original draft preparation, J.-K.L. (Jae-Kun Lee) and J.-K.L. (Jong-Kwon Lee) All authors have read and agreed to the published version of the manuscript.

Funding: This research was supported by the National Research Foundation of Korea (NRF) grant (2021R1A2C2014098), funded by the Ministry of Science and ICT of Korea.

Institutional Review Board Statement: Not applicable.

Informed Consent Statement: Not applicable.

Data Availability Statement: Data and materials can be made available upon request to the authors.

Conflicts of Interest: The authors declare no conflict of interest.

References

1. Côté, G.; Lalonde, J.-F.; Thibault, S. Extrapolating from lens design databases using deep learning. *Opt. Express* **2019**, *27*, 28279–28292. [CrossRef] [PubMed]
2. Zuo, C.; Qian, J.; Feng, S.; Yin, W.; Li, Y.; Fan, P.; Han, J.; Qian, K.; Chen, Q. Deep learning in optical metrology: A review. *Light Sci. Appl.* **2022**, *11*, 39. [CrossRef]
3. Sahin, F.E. Long-Range, High-Resolution Camera Optical Design for Assisted and Autonomous Driving. *Photonics* **2019**, *6*, 73. [CrossRef]
4. Makhataeva, Z.; Varol, H.A. Augmented Reality for Robotics: A Review. *Robotics* **2020**, *9*, 21. [CrossRef]
5. Kukkala, V.K.; Tunnell, J.; Pasricha, S.; Bradley, T. Advanced Driver-Assistance Systems: A Path Toward Autonomous Vehicles. *IEEE Consum. Electron. Mag.* **2018**, *7*, 18–25. [CrossRef]
6. Silva, V.D.; Roche, J.; Kondoz, A. Fusion of LiDAR and Camera Sensor Data for Environment Sensing in Driverless Vehicles. Loughborough University. Available online: https://hdl.handle.net/2134/33170 (accessed on 8 July 2022).
7. Rasshofer, R.H.; Spies, M.; Spies, H. Influences of weather phenomena on automotive laser radar systems. *Adv. Radio Sci.* **2011**, *9*, 49–60. [CrossRef]
8. Optical Glass for Automotive Cameras. Available online: https://www.oharacorp.com/optical-glass-for-automotive-cameras.html (accessed on 8 July 2022).
9. Available online: http://www.hoya-opticalworld.com/english/news/index.html (accessed on 24 August 2022).
10. Xiao, Z.; Yu, S.; Li, Y.; Ruan, S.; Kong, L.B.; Huang, Q.; Huang, Z.; Zhou, K.; Su, H.; Yao, Z.; et al. Materials development and potential applications of transparent ceramics: A review. *Mater. Sci. Eng. R Rep.* **2020**, *139*, 100518. [CrossRef]
11. Fahrenholtz, W.G.; Hilmas, G.E. Ultra-high temperature ceramics: Materials for extreme environments. *Scr. Mater.* **2017**, *129*, 94–99. [CrossRef]
12. Wuchina, E.; Opila, E.; Opeka, M.; Fahrenholtz, W.; Talmy, I. UHTCs: Ultra-High Temperature Ceramic Materials for Extreme Environment Applications. *Electrochem. Soc. Interface.* **2007**, *16*, 30–36. [CrossRef]
13. Heiroth, S.; Ghisleni, R.; Lippert, T.; Michler, J.; Wokaun, A. Optical and mechanical properties of amorphous and crystalline yttria-stabilized zirconia thin films prepared by pulsed laser deposition. *Acta Mater.* **2011**, *59*, 2330–2340. [CrossRef]
14. Krell, A.; Klimke, J.; Hutzler, T. Transparent compact ceramics: Inherent physical issues. *Opt. Mater.* **2009**, *31*, 1144–1150. [CrossRef]
15. Nazir, M.A.; Mahmood, T.; Zafar, A.A.; Akhtar, N.; Hussain, T.; Saeed, M.A.; Aleem, F.; Saeed, A.; Raza, J.; Cao, C. Electronic, optical and elastic properties of cubic zirconia (c-ZrO_2) under pressure: A DFT study. *Physica B* **2021**, *604*, 412462. [CrossRef]
16. Iosif, L.; Barbinta-Patrascu, M.E.; Ispas, A. Zirconia, from optoelectronics to oral environment applicability. *J. Optoelectron. Adv. Mater.* **2020**, *22*, 635–646.
17. Wang, C.; Mao, X.; Peng, Y.-P.; Jiang, B.; Fan, J.; Xu, Y.; Zhang, L.; Zhao, J. Preparation and Optical Properties of Infrared Transparent 3Y-TZP Ceramics. *Materials* **2017**, *10*, 390. [CrossRef] [PubMed]
18. Horti, N.C.; Kamatagi, M.D.; Nataraj, S.K.; Wari, M.N.; Inamdar, S.R. Structural and optical properties of zirconium oxide (ZrO_2) nanoparticles: Effect of calcination temperature. *Nano Express* **2020**, *1*, 010022. [CrossRef]
19. Lomonova, E.E.; Osiko, V.V. *Growth of Zirconia Crystals by Skull-Melting Technique*; John Wiley & Sons, Ltd.: Hoboken, NJ, USA, 2003.
20. Xu, J.; Lei, X.; Jiang, X.; He, Q.; Fang, Y.; Zhang, D.; He, X. Industrial growth of yttria-stabilized cubic zirconia crystals by skull melting process. *J. Rare Earths* **2009**, *27*, 971–974. [CrossRef]

21. Borik, M.A.; Bredikhin, S.I.; Bublik, V.T.; Kulebyakin, A.V.; Kuritsyna, I.E.; Lomonova, E.E.; Milovich, P.O.; Myzina, V.A.; Osiko, V.V.; Ryabochkina, P.A.; et al. Structure and conductivity of yttria and scandia-doped zirconia crystals grown by skull melting. *J. Am. Ceram. Soc.* **2017**, *100*, 5536. [CrossRef]
22. Kim, H.; Moon, J.Y.; Lee, J.-H.; Lee, J.-K.; Heo, Y.-W.; Kim, J.-J.; Lee, H.S. Transmission Electron Microscopy Study of 3.2 YSZ Single Crystals Manufactured by the Skull Melting Method. *J. Nanosci. Nanotechnol.* **2014**, *14*, 7961. [CrossRef]
23. Berendts, S.; Eufinger, J.-P.; Valov, I.; Janek, J.; Lerch, M. Ionic conductivity of low yttria-doped cubic zirconium oxide nitride single crystals. *Solid State Ion.* **2016**, *296*, 42–46. [CrossRef]
24. Suárez, M.; Fernández, A.; Menéndez, J.L.; Torrecillas, R.; Kessel, H.U.; Hennicke, J.; Kirchner, R.; Kessel, T. Challenges and Opportunities for Spark Plasma Sintering: A Key Technology for a New Generation of Materials. *Sinter. Appl.* **2013**, *13*, 319–342.
25. Paygin, V.; Stepanov, S.; Dvilis, E.; Khasanov, O.; Alishin, T.; Valiev, D. Effect of technological parameters on optical and mechanical properties of SPS transparent YSZ ceramics. *Ceram. Int.* **2021**, *47*, 11169–11175. [CrossRef]
26. Paygin, V.; Dvilis, E.; Stepanov, S.; Khasanov, O.; Valiev, D.; Alishin, T.; Ferrari, M.; Chiasera, A.; Mali, V.; Anisimov, A. Manufacturing optically transparent thick zirconia ceramics by spark plasma sintering with the use of collector pressing. *Appl. Sci.* **2021**, *11*, 1304. [CrossRef]
27. Peuchert, U.; Okano, Y.; Menke, Y.; Reichel, S.; Ikesue, A. Transparent cubic-ZrO_2 ceramics for application as optical lenses. *J. Eur. Ceram. Soc.* **2009**, *29*, 283. [CrossRef]
28. Papynov, E.K.; Shichalin, O.O.; Medkov, M.A.; Grishchenko, D.N.; Tkachenko, I.A.; Fedorets, A.N.; Pechnikov, V.S.; Golub, A.V.; Buravlev, I.Y.; Tananaev, I.G.; et al. Spark Plasma Sintering of Special-Purpose Functional Ceramics Based on UO_2, ZrO_2, Fe_3O_4/α-Fe_2O_3. *Glass Phys. Chem.* **2018**, *44*, 632–640. [CrossRef]
29. Papynov, E.K.; Shichalin, O.O.; Mayorov, V.Y.; Modin, E.B.; Portnyagin, A.S.; Tkachenko, I.A.; Belov, A.A.; Gridasova, E.A.; Tananaev, I.G.; Avramenko, V.A. Spark Plasma Sintering as a high-tech approach in a new generation of synthesis of nanostructured functional ceramics. *Nanotechnol. Russ.* **2017**, *12*, 49. [CrossRef]
30. Zhang, Z.H.; Liu, Z.-F.; Lu, J.-F.; Shen, X.-B.; Wang, F.-C.; Wang, Y.-D. The sintering mechanism in spark plasma sintering–Proof of the occurrence of spark discharge. *Scr. Mater.* **2014**, *81*, 56. [CrossRef]
31. Tsukerman, S.A. *Powder Metallurgy*; Elsevier: Amsterdam, The Netherlands, 1965.
32. Langer, J.; Hoffmann, M.J.; Guillon, O. Electric Field-Assisted Sintering in Comparison with the Hot Pressing of Yttria-Stabilized Zirconia. *J. Am. Ceram. Soc.* **2011**, *94*, 24. [CrossRef]
33. Mondal, P.; Klein, A.; Jaegermann, W.; Hahn, H. Enhanced specific grain boundary conductivity in nanocrystalline Y_2O_3-stabilized zirconia. *Solid State Ion.* **1999**, *118*, 331. [CrossRef]
34. Hu, C.; Li, F.; Qu, D.; Wang, Q.; Xie, R.; Zhang, H.; Peng, S.; Bao, Y.; Zhou, Y. Developments in hot pressing (HP) and hot isostatic pressing (HIP) of ceramic matrix composites. In *Advances in Ceramic Matrix Composites*; Elsevier: Amsterdam, The Netherlands, 2014.
35. Available online: https://www.kobelco.co.jp/english/products/ip/technology/hip.html (accessed on 24 August 2022).
36. Dash, A.; Kim, B.-N.; Klimke, J.; Vleugels, J. Transparent tetragonal-cubic zirconia composite ceramics densified by spark plasma sintering and hot isostatic pressing. *J. Eur. Ceram. Soc.* **2019**, *39*, 1428. [CrossRef]
37. Ergun, C. Enhanced phase stability in hydroxylapatite/zirconia composites with hot isostatic pressing. *Ceram. Int.* **2011**, *37*, 935–942. [CrossRef]
38. Lach, R.; Bućko, M.M.; Haberko, K.; Sitarz, M.; Cholewa-Kowalska, K. From nanometric zirconia powder to transparent polycrystal. *J. Eur. Ceram. Soc.* **2014**, *34*, 4321. [CrossRef]
39. Guo, J.; Floyd, R.; Lowum, S.; Maria, J.-P.; Beauvoir, T.H.; Seo, J.-H.; Randall, C.A. Cold Sintering: Progress, Challenges, and Future Opportunities. *Annu. Rev. Mater. Res.* **2019**, *49*, 275. [CrossRef]
40. Grasso, S.; Biesuz, M.; Zoli, L.; Taveri, G.; Duff, A.I.; Ke, D.; Jiang, A.; Reece, M.J. A review of cold sintering processes. *Adv. Appl. Ceram.* **2020**, *119*, 115. [CrossRef]
41. Maca, K.; Pouchly, V.; Zalud, P. Two-Step Sintering of oxide ceramics with various crystal structures. *J. Eur. Ceram. Soc.* **2010**, *30*, 583. [CrossRef]
42. Guo, H.; Bayer, T.J.M.; Guo, J.; Baker, A.; Randall, C.A. Cold sintering process for 8 mol%Y_2O_3-stabilized ZrO_2 ceramics. *J. Eur. Ceram. Soc.* **2017**, *37*, 2303. [CrossRef]
43. Vasanthavel, S.; Kannan, S. Structural investigations on the tetragonal to cubic phase transformations in zirconia induced by progressive yttrium additions. *J. Phys. Chem.* **2018**, *112*, 100. [CrossRef]
44. Ray, J.C.; Pati, R.K.; Pramanik, P. Chemical synthesis and structural characterization of nanocrystalline powders of pure zirconia and yttria stabilized zirconia (YSZ). *J. Eur. Ceram. Soc.* **2000**, *20*, 1289. [CrossRef]
45. Krogstad, J.A.; Lepple, M.; Gao, Y.; Lipkin, D.M.; Levi, C.G. Effect of Yttria Content on the Zirconia Unit Cell Parameters. *J. Am. Ceram. Soc.* **2011**, *94*, 4548. [CrossRef]
46. Pai Verneker, V.R.; Petelin, A.N.; Crowne, F.J.; DC Nagle, D.C. Color-center-induced band-gap shift in yttria-stabilized zirconia. *Phys. Rev. B.* **1989**, *40*, 8555. [CrossRef]
47. Dombrovsky, L.A.; Rousseau, B.; Echegut, P.; Randrianalisoa, J.H.; Baillis, D. High Temperature Infrared Properties of YSZ Electrolyte Ceramics for SOFCs: Experimental Determination and Theoretical Modeling. *J. Am. Ceram. Soc.* **2011**, *94*, 4310–4316. [CrossRef]

48. Yamashita, I.; Kudo, M.; Tsukuma, K. Development of highly transparent zirconia ceramics. *TOSOH Res. Techno. Rev.* **2012**, *56*, 11–16.
49. Orliukas, A.; Bohac, P.; Sasaki, K.; Gauckler, L.J. The relaxation dispersion of the ionic conductivity in cubic zirconia. *Solid State Ion.* **1994**, *72*, 35–38. [CrossRef]
50. Wood, D.L.; Nassau, K. Refractive index of cubic zirconia stabilized with yttria. *Appl. Optics* **1982**, *21*, 2978–2981. [CrossRef]
51. Juškevičius, K.; Audronis, M.; Subačius, A.; Drazdys, R.; Juškenas, R.; Matthews, A.; Leyland, A. High-rate reactive magnetron sputtering of zirconia films for laser optics applications. *Appl. Phys. A* **2014**, *116*, 1229–1240. [CrossRef]
52. Jenkins, F.A.; White, H.E. *Fundamentals of Optics*; Tata McGraw-Hill Education: New York, NY, USA, 1937.
53. Ohara Catalog. Available online: https://www.oharacorp.com/catalog.html (accessed on 8 July 2022).
54. Steimacher, A.; Medina, A.N.; Bento, A.C.; Rohling, J.H.; Baesso, M.L.; Reynoso, V.C.S.; Lima, S.M.; Petrovich, M.N.; Hewak, D.W. The temperature coefficient of the optical path length as a function of the temperature in different optical glasses. *J. Non-Cryst. Solids.* **2004**, *348*, 240–244. [CrossRef]
55. Tropf, W.J.; Harris, T.J.; Thomas, M.E. Optical materials: Visible and infrared. In *Electro-Optics Handbook*; The McGraw-Hill Companies, Inc.: New York, NY, USA, 2000.
56. Nuno, K.; Sugiura, K.; Ohashi, K. Lens Barrel, Camera and Mobile Information Terminal. U.S. Patent 8537478B2, 17 September 2013.